Modelling of a falling film evaporator for adsorption chillers.

Marcello Aprile ([1,a]), A.J. Di Cicco[a], T. Toppi[a], A. Freni[b], M. Motta[a,b]

[a] Department of Energy, Politecnico di Milano, 20156 Milano, Italy

[b] CNR - Institute of Chemistry of Organo Metallic Compounds (ICCOM), Pisa, Italy

Preprint.

Please cite this paper as:

M. Aprile, A.J. Di Cicco, T. Toppi, A. Freni, M. Motta. Modelling of a falling film evaporator for adsorption chillers. International Journal of Refrigeration 146 (2023), 471 – 482. https://doi.org/10.1016/j.ijrefrig.2022.12.009

Abstract

The objective of the present study was to develop a dynamic model to simulate a prototype falling-film evaporator that is part of a single-bed adsorption chiller test bench located at the Department of Energy of the Politecnico di Milano. The model is based on evaporator energy and mass balances and was calibrated and validated using experimental data coming from realistic operating conditions in a range of inlet chilled water temperatures ($T_{in,chw}$) from 15 to 25 °C. From the experimental data, it was obtained that the average overall heat transfer conductance (UA) was approximately 530 W/K for all temperatures during the quasi steady-state section of the process. A correlation to calculate the wetted surface through a variable called wettability factor (f_{wet}) was developed from experimental data. The f_{wet} factors were identified using the model and were in the range of 0.80 – 0.20 ($T_{in,chw}$ = 15 °C) and 0.60 – 0.20 ($T_{in,chw}$ = 25 °C). It was seen

[1] Corresponding author

E-mail address: marcello.aprile@polimi.it

that, the higher the $T_{in,chw}$, the lower the f_{wet} values. The UA and saturation temperature ($T_{ref,sat}$) values from the model were in good accordance with experimental data during the quasi steady-state section of the process. Nevertheless, the final transition stage (a situation in which, for single-bed adsorption chillers, the evaporator's refrigerant pool is empty) required an additional hypothesis due to the uncertainty of the process' dynamics when no more recirculated flowrate falls on top of the tubes. The mass and energy balances that are part of the hydrodynamics and heat transfer sections of the model use Nusselt's classic theory for falling-film.

1. Introduction

Adsorption chillers can rely on waste heat and/or solar collectors as heat source. This represents an important characteristic for this kind of chillers because they are able to use low-temperature heat sources (temperatures lower than 90 °C) for functioning. This advantage makes them an interesting technology for different applications, such as air conditioning, solar cooling, industrial refrigeration, cold storage, and desalination (Mitra et al. (2014); Chauhan et al. (2022)). Furthermore, another advantage for adsorption chillers is the fact that water can be used as refrigerant. The main components of an adsorption chiller are the evaporator, sorption beds and the condenser. Adsorption chillers generally work in two modes: adsorption/evaporation and desorption/condensation, meaning that they are characterized by a transient operation. Therefore, the most common configuration of an adsorption chiller includes two sorption beds, one connected to the evaporator for adsorption/evaporation and the second one connected to the condenser for desorption/condensation. Both beds switch their connections between the evaporator and condenser continuously depending on their working mode. Details on principle and operation of the basic sorption cooling cycle can be found elsewhere (Ziegler (2009)). More complex adsorption cycles, based on multiple adsorbent beds and different heat and mass transfer recovery schemes, have been proposed to improve the adsorption chiller thermodynamic performance (Aprile et al. (2020); Muttakin et al. (2021)).

An important component of this heat pump is the evaporator, and its proper functioning can represent a bottleneck situation for the entire system (Lee et al. (2020)). As previously mentioned, water can be used as refrigerant for adsorption heat pumps, forcing the evaporator to work in sub-atmospheric conditions (pressures that can be in the range 0.5 – 5 kPa (Thimmaiah et al. (2017))). Consequently, small pressure

variations can alter the operation of the evaporator. Furthermore, a low heat transfer coefficient from the evaporator's side leads to a higher temperature difference between the tube's wall and the refrigerant water; this means that both the evaporator and adsorption bed would suffer a decrease in the working pressure, penalizing the adsorption process.

Adsorption chillers can be coupled with evaporators that use as heat transfer mechanism either pool boiling (Thimmaiah et al. (2017)) or falling-film (Toppi et al. (2022)). Flooded evaporators require that the tubes are completely immersed in the refrigerant pool; on the other hand, falling-film evaporators use a system in which the refrigerant is sprayed on top of the tubes, forming a layer of film on the tubes' surfaces. Falling-film evaporators have important advantages over their pool boiling counterparts, such as lower amount of refrigerant load, smaller and more compact design (costs reduction) and higher heat transfer coefficient (Ribatski and Jacobi (2005)).

Regardless of these advantages, the main aspect that can alter the operation of falling-film evaporators in adsorption chillers is the liquid distribution on the tubes bundle. This is because a bad liquid distribution can give rise to surface dryout, affecting the heat exchange area, which is the wetted surface (Ribatski and Thome (2007)). The fluid distribution across the tubes can also be affected by the continuous evaporation of refrigerant, leading to the formation of dry patches and reduction in the wetted area. This, in turn, also means a reduction of the heat transfer coefficient, worsening the heat transfer process (Ribatski and Thome (2007)).

Falling-film evaporators and adsorption chillers have been investigated in literature from an experimental and theoretical point of view. Volmer et al. (2017) studied from an experimental and theoretical point of view the evaporation dynamics of a tube-fin evaporator, studying both thin film and flooded evaporation at sub-atmospheric conditions. When explaining the behavior of the UA curves, they highlighted that the initial section was characterized by a good thermal contact between the fluid and the tubes' surfaces; however, they pointed out that the following plateau section was due to refrigerant being held in the spaces between fins by capillary forces. They also developed a model based on thermal resistances to simulate the thin film evaporation and validated it against experimental data.

Ammar and Park (2021) tested a falling film evaporator for an absorption refrigeration system with seven different small-diameter tubes to understand how enhanced surfaces could improve the evaporator's wetting and performance. They estimated film Reynolds numbers in the range from 10 to 100 and worked with sub-

atmospheric saturation pressure in the range of 0.93 to 1.20 kPa, and obtained that the increase of the saturation pressure led to an increase of the heat transfer coefficient due to the decrease of film's viscosity (thinner film).

The prediction of the evolution of the wetted surface of a falling-film evaporator is a topic that has also been investigated in literature. Ribatski and Thome (2007) investigated the onset of local dryout of falling-film with nucleate boiling using saturated R134a as refrigerant, and they proposed a correlation to calculate the fraction of wetted area as a function of the film Reynolds number. From their results, they obtained that the decrease of the wetted area affects the heat transfer coefficient. Bustamante et al. (2020b) developed a model to simulate a falling-film evaporator with rectangular tubes using Nusselt's classic theory for falling-film. Moreover, they also developed a correlation to calculate the fraction of wetted surface as a function of Reynolds number, modified Galileo number and geometric aspects of their falling-film evaporator. Yang et al. (2017) obtained in their simulation that the falling-film evaporation performance worsened as the dry patches increased. He et al. (2021) presented a mathematical model for the prediction of dry patches on falling-film considering the evaporation of film from the tube's surface. They obtained that the increase of film flow rate delayed the formation of dry patches, and that they appeared earlier in the surface with the increase of the spray temperature. De la Calle et al. (2012) developed a model to simulate a horizontal tube falling film evaporator using as background theory Newton's viscosity law and Nusselt's falling-film theory. The evaporator the authors modeled is part of a double-effect absorption heat pump that, at the same time, is coupled to a solar thermal multi-effect distillation system. Furthermore, they also included the wetted surface calculation using as reference the work from Habert and Thome (2010). In a separate publication, De la Calle et al. (2013) changed their approach and, instead of using Nusselt's conduction model, they opted to use correlations from literature.

Another section of the literature review was focused on the analysis of different correlations to calculate the film heat transfer coefficient (h_{film}) and to check how the wettability of the tube may influence these correlations. Moreover, the regime under which these correlations were developed was also considered. To name a few, Chun & Seban (1971) proposed a correlation after studying an electrically heated vertical tube, using as working fluid pure water. The Chun & Seban (1971) correlation was empirically developed for the prediction of the film heat transfer coefficient in both laminar and turbulent regimes. The empirical

correlations from Chun & Seban (1971) can be used for the prediction of laminar and turbulent heat transfer coefficients for vertical tubes (in the fully developed region); moreover, they do not contemplate nucleate boiling, but film convection. Han & Fletcher (1985) proposed correlations for circumferential and axial grooves horizontal tubes, studying the turbulent regime. They concluded that, on the turbulent regime, the film heat transfer coefficient increases with both, saturation temperature and flowrate, leading them to write a correlation with a direct relationship between h_{film} and the film Reynolds number (Re_Γ). Moreover, their correlations were developed under a Re_Γ range of $770 \leq Re_\Gamma \leq 7000$. Owens (1978) proposed a correlation to predict thin film heat transfer coefficient for horizontal tubes using experimental data from ammonia and water. The correlation presented by Owens (1978) for non-boiling film evaporation for laminar range used data from ammonia only. The Reynolds number dependance that Owens (1978) found was the same as the one from Nusselt's works on condensation. Alhusseini et al. (1998) also developed a falling film heat transfer correlation using, as working fluids, water, and propylene glycol (their set-up included an electrically heated vertical tube). Alhusseini et al. (1998) presented their results with experimental Re_Γ values in the ranges of 416 – 15600, 139 – 8600 and 190 – 6527 (all of them obtained with water as working fluid and for temperatures between 99.6 and 38.5 °C). Furthermore, they also obtained that, for laminar films with low Re_Γ values, the Nusselt number decreased with the increase of the film Reynolds number. For the case of turbulent regimes, they obtained that the Nusselt number increased with increasing Re_Γ . This allowed them to conclude that there was a critical Reynolds between 400 and 3000 for the transition between laminar and turbulent regime. In their model, Bustamante et al. (2020b) calculated a heat transfer coefficient starting from Nusselt's film theory, also including the wetting ratio, to account for the wetted area (the authors reported Reynolds numbers below 600).

The change from laminar to turbulent regime has been highlighted by several authors, and the working regime influences the choice of the heat transfer correlation. Ding et al. (2018) worked on a CFD model for falling film on horizontal tubes based on the volume of fluid method and assumed a laminar thin film liquid flow because the Reynolds numbers were lower than 500. Tahir et al. (2021) carried out the development and validation of a 2D model for the simulation of a multi-effect evaporator with horizontal tubes. For their model, the authors considered a laminar flow with a maximum Reynolds number of 460. On their literature review, Ouldhadda and Il Idrissi (2001) highlighted that, according to Mitrovic (1986) and Ganic and Roppo

(1980), the fluid is laminar if the Reynolds number is lower than 315; also, Ouldhadda and Il Idrissi (2001) wrote that, according to Parken and Fletcher (1982) and Ueda and Tanaka (1975), the transition from laminar to turbulent flow corresponds to Reynolds between 4000 and 6000.

Chyu and Bergles (1987) studied falling film heat transfer on horizontal smooth tubes and developed two models based on four heat transfer regions outside the tubes. The four heat transfer regions according to Chyu and Bergles (1987) are: stagnation flow, jet impingement region, thermal developing region (heat is transferred to superheat the film flow) and the fully developed region (the film flow is characterized by a linear temperature profile). For the thermal developing region, Chyu and Bergles (1987) assumed, in their analysis that the film flow was considered laminar, and the heat transfer is only by conduction across the film. Chyu and Bergles (1987) calculated the heat transfer coefficient for the fully developed zone in two ways: the first one with the heat conduction solution, while the second one was by means of the Chun and Seban (1972) correlation. Chyu and Bergles (1987) explained that, at low film flow rates, the major contribution to the overall heat transfer coefficient comes from the fully developed region, while the contribution from the jet impingement region is only a small fraction because this is a small region.

Sarma and Saibabu (1992) conducted an analytical study of laminar falling film evaporation on a horizontal tube with constant wall heat flux. They considered an approach like Chyu and Bergles (1987), in which the falling film heat transfer is calculated with contributions from different regions. The first heat transfer region considered by Sarma and Saibabu (1992) was a zone of film superheating with negligible evaporation. The second heat transfer stage considered simultaneous superheating and evaporation while the third one was characterized by a linear temperature profile and all heat conducted from the wall is meant for evaporation. Sarma and Saibabu (1992) proposed a correlation for laminar falling film where the average heat transfer coefficient is inversely proportional to the film Reynolds number. The Reynolds range for this correlation was $200 < Re_{\Gamma} < 1500$. Regarding the link with the peripheral angel, Sarma and Saibabu (1992) reported that the zone of evaporation begins at an angle near 50° for a Re_{Γ} of 200, while a Re_{Γ} of 500 means that the zone of evaporation begins at almost 130°.

According to literature review, the formation of dry patches is an important aspect to consider in the operation of falling-film evaporators. Even though a falling-film evaporator can provide more advantages compared to a flooded evaporator and, furthermore, it can effectively be inserted in an adsorption heat pump

with water as refrigerant (Toppi et al. (2022)), its performance can be negatively affected by a deficient amount of film flow rate and mass of film on top of the tubes. For the heat pump configuration used to validate the mathematical model in this article, this decline in performance was commented in Toppi et al. (2022) through the evolution of the overall heat transfer conductance (UA) during the evaporation process. The UA conductance includes the contributions of each individual thermal resistance involved in the process, and, moreover, contains the wetted surface (considered to be the exchange area). Toppi et al. (2022) noted that the UA conductance decreased continuously as less refrigerant water fell on top of the tubes bundle (also decreasing the heat transfer flux between the chilled water and the refrigerant film).

Consequently, the dynamic relationship between the heat transfer process and the wetted surface is an aspect that must be addressed in any experimental or theoretical study regarding falling-film evaporators for adsorption heat pumps.

The main objective of this study is to develop a dynamic model to fully characterize the performance of a prototype falling-film evaporator that is part of an experimental adsorption chiller located at the Department of Energy of the Politecnico di Milano. Several tests were performed on this adsorption heat pump, and the collected experimental data was then used for the development and validation of a dynamic model able to simulate the evaporation process.

The novelty of this study relies on the fact that the model was developed and validated against experimental data coming from realistic operating conditions of an adsorption chiller. This means that the transient nature of the process during sub-atmospheric conditions and the interaction between the falling-film evaporator and adsorption bed can be characterized, not only from an experimental point of view, but also from a theoretical point of view. This transient operation includes the initial stage with the valve opening as well as the final transition phase when the recirculated flowrate stops arriving at the top of the evaporator and the final fraction of film on top of the tubes is evaporated.

Moreover, another contribution from the present study is the development of an empirical correlation that predicts the evolution of the wetted surface for this prototype falling-film evaporator. This is of high importance because the proper evaluation of the wetted surface allows to obtain, from the model, a realistic prediction of evaporation dynamics behavior.

The evolution of the wetted surface is analyzed through a variable called wettability factor (f_{wet}), which represents the ratio between the wetted surface to the total exchange area and has an important influence in the entire process. The f_{wet} values were identified using the model with experimental data coming from tests performed with an inlet chilled water temperature ($T_{in,chw}$) range from 15 to 25 °C. The f_{wet} values were fitted into a correlation as a function of the Reynolds and Prandtl numbers, to highlight its link with the refrigerant's mass of film as well as its temperature and viscosity.

2. Experimental methods

The data used for the calibration and validation of the model comes from tests performed on an adsorption chiller test bench located at the Department of Energy of the Politecnico di Milano. In this section, the test bench (which was used by Toppi et al. (2022) on a separate research focused on the prototype falling-film evaporator) is presented as well as the methodology used to collect the experimental data.

2.1 Experimental set-up

The used single-bed adsorption chiller is composed by a falling-film evaporator, condenser, and adsorbent bed. It is connected to three hydraulic circuits (cold water, hot water, and intermediate circuit) that act as the external sources/sink and provide the necessary water flows at given set temperatures. These external sinks have nominal capacities of 2 kW (for the evaporator and condenser) and 5 kW (for the adsorbent bed), with water flowrates in the range 200 – 1000 L/h. The adsorption bed contains granular RD silica gel that is embedded in a finned heat exchanger. The falling-film evaporator is composed of stainless-steel tubes divided into two coils, with six tubes per coil. The outside surface of the tubes is corrugated to provide a fin-like structure and to better distribute the film as it falls on the outside of the tubes. Figure 1 presents different views from a CAD model of the evaporator to see its internal structure. From Figure 1.a and 1.b, it can be stated that the water enters in the lower tube and exits from the top tube. Moreover, the orange tube in Figures 1.a and 1.b is the tube responsible for spraying the refrigerant. Figure 2 presents a picture of the outside surface of the tubes (seen from a small window in the evaporator's case) to visualize the corrugated surface and the channels that guide the refrigerant on the outside surface on each tube.

The refrigerant water is distributed in four sections of the system, being the refrigerant pool, pump's suction and discharge tubes and the film accumulated on the tubes' bundle. The adsorption test bench is shown in Figure 3.a, while the schematic of the refrigerant mass distribution inside of the evaporator is presented in Figure 3.b.

The test bench is equipped with Pt 100 resistance temperature sensors to measure the inlet/outlet temperatures of each component (Pt 100 1/10 DIN class, range: -10 – 100 °C, accuracy: ± 0.03 °C at 0 °C). Pressure transmitters monitor the vapor pressures from each component (range: 0 – 20 kPa, accuracy: 0.25 % of reading), while magnetic flowmeters are used to measure the water flowrates (range 200 – 1000 L/h, accuracy < 0.5 % of reading). The evaporator's recirculated flowrate is measured by an ultrasonic flowmeter (range 0 – 600 L/h, accuracy ± 3 % of reading). A more detailed and expanded explanation of the chiller set-up configuration and hydraulic circuits can be found in Toppi et al. (2022). The three components work at sub-atmospheric conditions, and a vacuum pump is used to purge the non-condensable gases from each component.

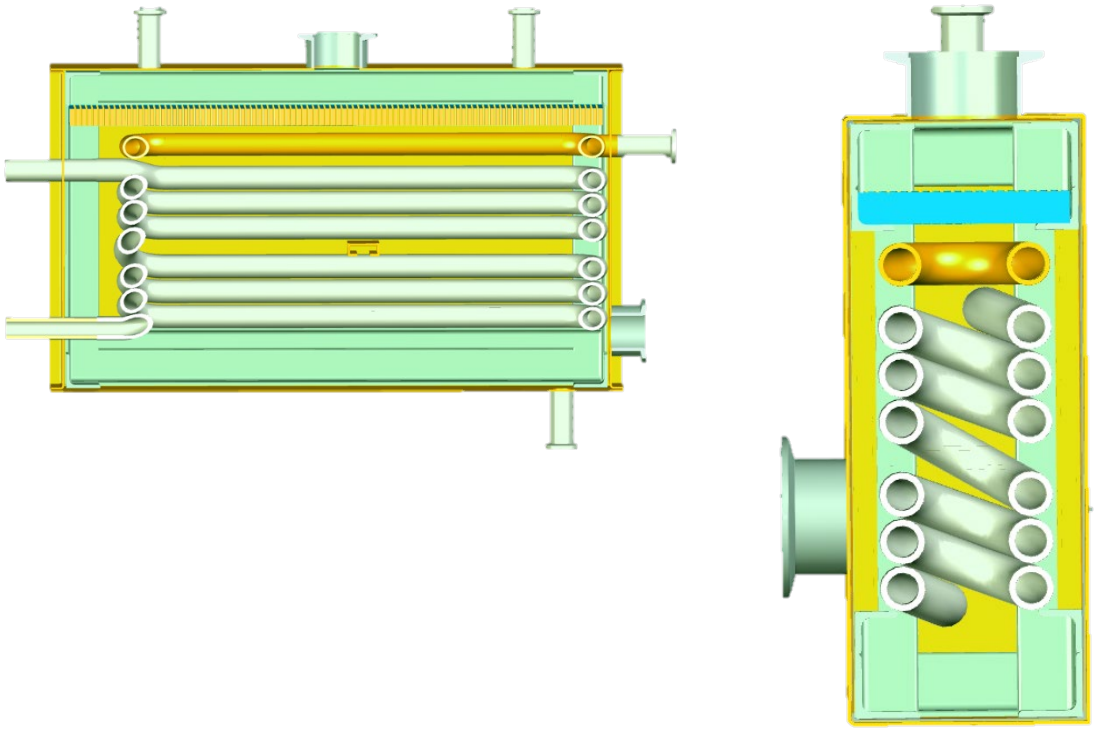

(a) (b)

Figure 1 – Falling-film evaporator CAD model: front view section (a) and side view section (b).

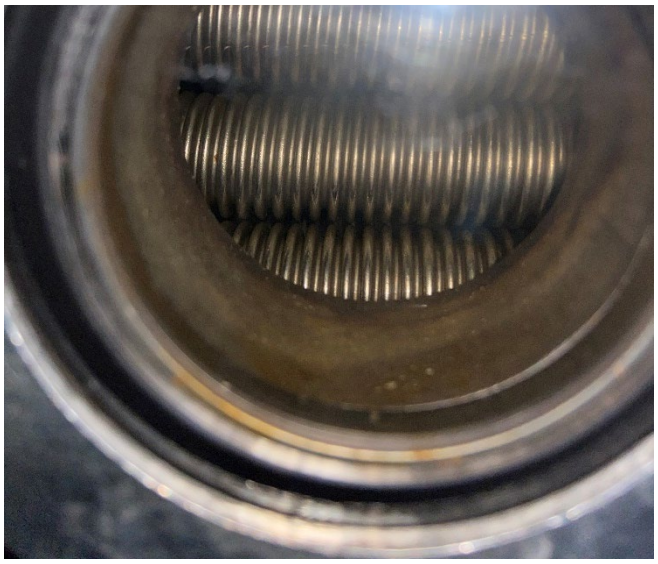

Figure 2 – Tubes corrugated surface.

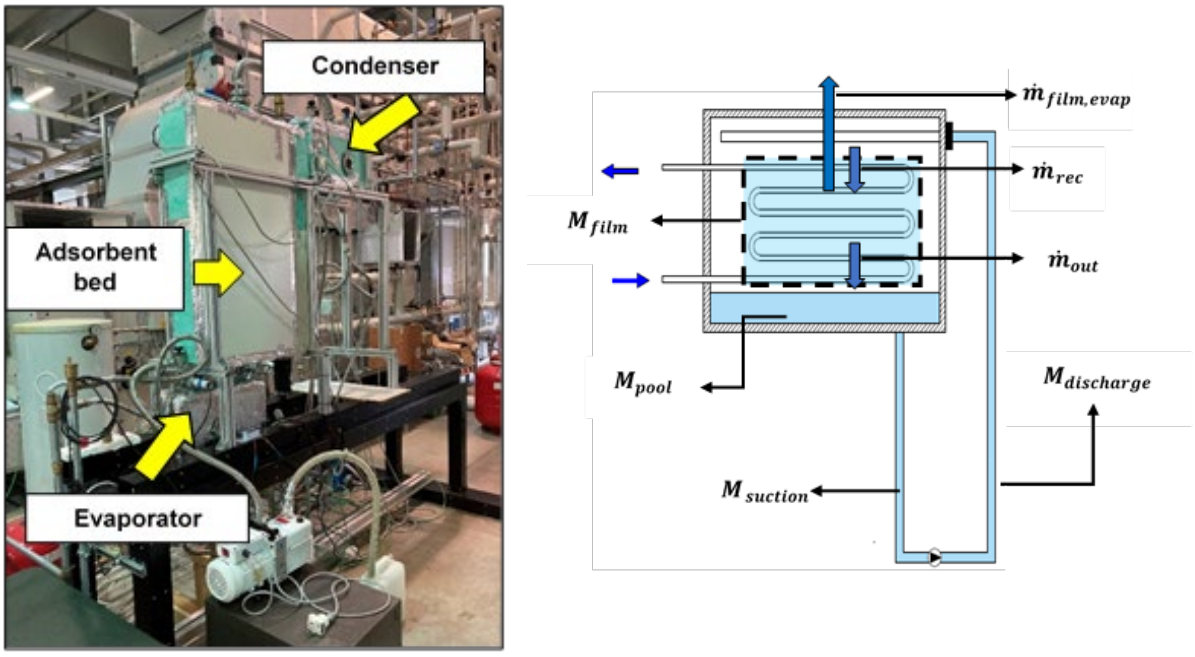

(a) (b)

Figure 3 – Adsorption chiller experimental set-up (a) and evaporator refrigerant mass distribution (b).

2.2 Testing procedure and conditions

Since the test bench is a single-bed adsorption chiller, the evaporation and condensation processes cannot be carried out simultaneously. The experimental conditions are shown in Table 1, while the used testing methodology, divided into four phases, is explained as follows:

a. **Heating and desorption/condensation:** this process is schematically presented in Figure 4.a. The adsorption bed is connected to the hot water circuit (TH in Figure 4.a) to be isosterically heated up with hot water (90 °C) and increase the bed's pressure until reaching the one in the condenser. The valves connecting the evaporator and the condenser to the adsorption bed remains closed. Once the adsorbent's bed pressure reaches the condenser's pressure level, the valve connecting the adsorption bed to the condenser is opened to allow the desorbed vapor flow towards the condenser. The intermediate circuit (TM in Figure 4.a) is connected to the condenser for the desorbed vapor.

b. **Cooling and adsorption/evaporation:** this phase is visually shown in Figure 4.b. With the desorption/condensation phase over, the valve connecting them is closed and water from the intermediate circuit is circulated across the adsorption bed to decrease its pressure. Furthermore, at the same time, an amount of condensed water from the bottom of the condenser is discharged to the evaporator to create the refrigerant pool, and the recirculation system is turned on. When the minimum adsorption temperature is reached, the valve connecting the adsorption bed to the evaporator is opened, to begin the evaporation process. The recirculation system continues to circulate the refrigerant from the refrigerant pool to the top of the evaporator.

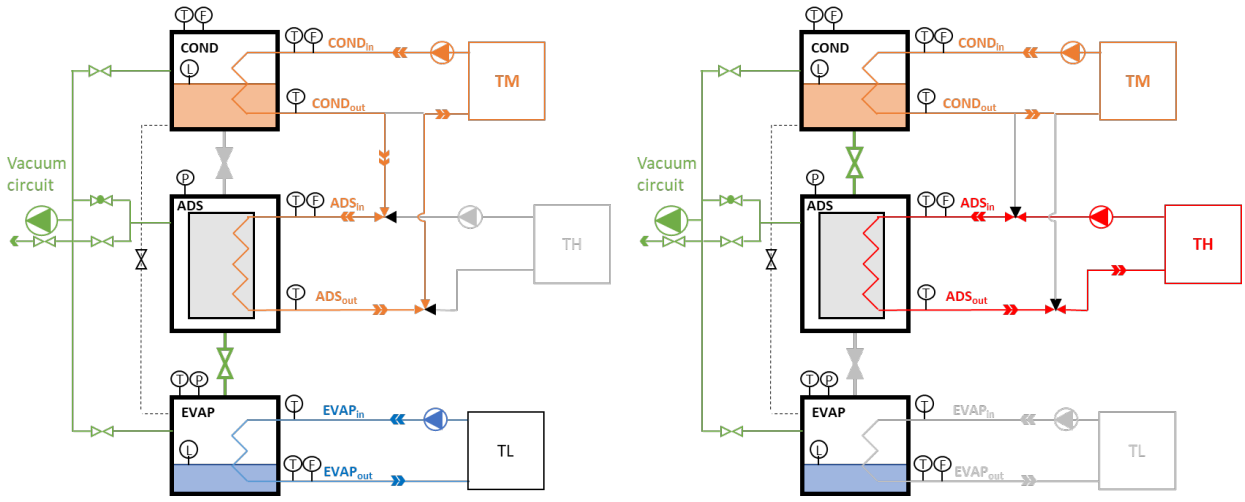

Figure 4 – Single-bed adsorption chiller working scheme: desorption/condensation (a) and adsorption/evaporation (b).

Table 1 – Experimental tests conditions.

$T_{in,chw}$ [°C]	$P_{ref,sat}$ [Pa]	$\dot{m}_{chw}$ [m^3/h]	$T_{water,ads}$ [°C]
15 – 25	1705 – 3171	0.4	25

2.3 Approach to the data analysis

For each test, the following quantities were measured with a timestep of one second: inlet chilled water temperature ($T_{in,chw}$), outlet chilled water temperature ($T_{out,chw}$), chilled water mass flowrate ($\dot{m}_{chw}$), refrigerant film saturation pressure ($P_{sat,ref}$) and refrigerant film recirculated flowrate ($\dot{m}_{rec}$). From these quantities, others were calculated. The heat flux removed from the chilled water by the refrigerant film (Q_{exp}) is calculated as presented in equation (1), while the evaporated flowrate ($\dot{m}_{film,evap}$) is shown in equation (2). Since the uncertainty of the wetted surface does not allow the calculation of the film heat transfer coefficient (h_{film}), the UA value is calculated as presented in equation (3), using the logarithmic mean temperature difference (ΔT_{LMTD}) shown in equation (4). The term $T_{ref,sat}$ in equation (4) refers to the refrigerant film saturation temperature.

$$Q_{exp} = \dot{m}_{chw} \cdot Cp_{chw} \cdot \left(T_{in,chw} - T_{out,chw}\right) \quad (1)$$

$$\dot{m}_{film,evap} = \frac{Q_{exp}}{h_{fg}} = \frac{\left(\dot{m}_{chw} \cdot Cp_{chw} \cdot \left(T_{in,chw} - T_{out,chw}\right)\right)}{h_{fg}} \quad (2)$$

$$UA = \frac{Q_{exp}}{\Delta T_{LMTD}} \quad (3)$$

$$\Delta T_{LMTD} = \frac{\left(T_{in,chw} - T_{ref,sat}\right) - \left(T_{out,chw} - T_{ref,sat}\right)}{Ln\left(\frac{T_{in,chw} - T_{ref,sat}}{T_{out,chw} - T_{ref,sat}}\right)} \quad (4)$$

3. Falling-film mathematical model

In this section, the developed falling-film model is explained. First, the refrigerant mass balances are shown, followed by the energy balances and the heat transfer equations. The f_{wet} identification feature is also presented to illustrate how the model calculates the f_{wet} factors for each timestep. This falling-film model solves, during each timestep, a system of nine ordinary differential equations that come from the evaporator's energy and mass balances. The ODE system includes also calculation of the volume, mass and temperature of the water vapour phase. The evaporation process is divided into two phases: a first phase of quasi steady-state conditions in which the refrigerant pool is present in the evaporator ($M_{pool} > 0$), and a second evaporation phase (final transitory stage) in which the heat transfer rate begins to decrease ($M_{pool} = 0$). Besides the initial conditions, the model requires primary inputs from experimental data, being the chilled water flowrate ($\dot{m}_{chw}$), inlet chilled water temperature ($T_{in,chw}$), and film evaporated flowrate ($\dot{m}_{film,evap}$).

A general flowchart of the model's working algorithm is presented in Figure 3. The equations used in the model are presented in the following sections, but the flowchart in Figure 3 presents a general idea of the model's working algorithm. After reading the experimental primary inputs and initial conditions, the model computes the refrigerant's properties as well as those from the chilled water (secondary inputs). By knowing the mass distribution and M_{film}, the wetted surface is estimated as well as the film's thickness ($\bar{\delta}_{film}$).

Finally, the model solves the heat transfer model by calculating the heat transfer coefficients, thermal resistances, UA value and heat transfer rate Q_{evap}. All of this information is used to solve the ODE system and get the initial conditions for the next timestep.

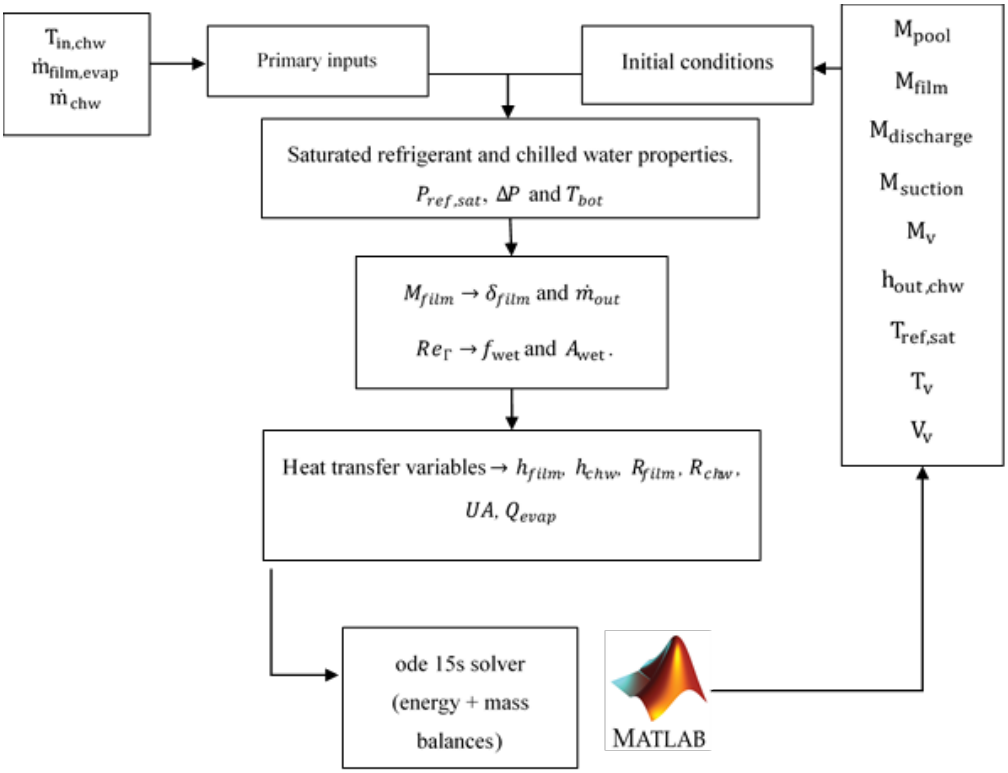

Figure 3 – Model flowchart.

3.1 Refrigerant mass balances

The differential mass balances were derived for each of the four refrigerant sections presented in Figure 3.b, and they are detailed in equations (5), (6), (7) and (8) for M_{pool}, M_{film}, $M_{suction}$ and $M_{discharge}$, respectively. The film's thickness of one tube is calculated using the mass of film (M_{film}), and it is presented in equation (9).

$$\frac{dM_{pool}}{dt} = \dot{m}_{out} - \dot{m}_{rec} \tag{5}$$

$$\frac{dM_{film}}{dt} = \dot{m}_{rec} - \dot{m}_{out} - \dot{m}_{film,evap} \tag{6}$$

$$\frac{dM_{suction}}{dt} = \begin{cases} 0, & M_{pool} > 0 \\ \dot{m}_{rec} - \dot{m}_{out}, & M_{pool} = 0 \end{cases} \tag{7}$$

$$\frac{dM_{discharge}}{dt} = 0 \tag{8}$$

$$\bar{\delta}_{film} = \frac{M_{film}}{12 \cdot A_{tube} \cdot f_{wet} \cdot \rho_l} \tag{9}$$

In equation (9), the term A_{tube} refers to the area of one tube, and it is multiplied by the total number of tubes, being twelve (see Figure 1.b). The term ρ_l refers to the saturated refrigerant liquid density. The term $\dot{m}_{out}$ is the flowrate falling to the pool from the final row of the tubes bundle (see Figure 3.b), and it's calculated with equation (10). Equation (10) was derived starting from the average film thickness from equation (9) and the use of Nusselt's equation for falling-film thickness (equation (11)).

It is important to point out that, as equation (11) suggests, the film thickness depends on the angular position (θ_i); for each tube, six angular positions were considered (from 30° to 180° in steps of 30°). The flow density term (Γ), which represents the mass flowrate of film flowing on one side of the tube, is presented in equation (12).

$$\dot{m}_{out} = 2 \cdot \left(\frac{\left(\bar{\delta}_{film}\right)^3 \cdot \rho_l \cdot (\rho_l - \rho_v) \cdot g \cdot 4 \cdot L_{tube} \cdot f_{wet}}{\left(\sum_{i=1}^{6} \left(\frac{1}{6}\right) \cdot \left(\frac{1}{\sin(\theta_i)}\right)^{\frac{1}{3}} \right)^3 \cdot 3 \cdot \mu_l} \right) \tag{10}$$

$$\delta_{film}(\theta_i) = \left(\frac{3 \cdot \mu_l \cdot \left(\frac{\Gamma}{f_{wet}}\right)}{\rho_l \cdot (\rho_l - \rho_v) \cdot g \cdot \sin(\theta_i)} \right)^{\frac{1}{3}} \tag{11}$$

$$\Gamma = \frac{\left(\frac{\dot{m}_{out}}{2}\right)}{2 \cdot L_{tube}} \tag{12}$$

In the previous equations, the terms $\mu_{ref,sat}$ and ρ_v refer, respectively, to the saturated refrigerant dynamic viscosity and vapor density. The variable g is the acceleration of gravity. In equations (10) and (12), L_{tube} is the length of one tube. The fact that equation (10) is re-organized from equations (9) and (11) means that the term $\dot{m}_{out}$ directly depends on M_{film}. In equation (11), the term Γ is divided by f_{wet} to highlight the fact that it is referred to a wetted length. The refrigerant recirculated flowrate ($\dot{m}_{rec}$) is calculated using empirical correlations developed with the experimental data from the performed tests (see Table 1) and using as reference the analyses from Toppi et al. (2022). The amount of refrigerant water used on each test was approximately 1.8 kg, which represents around 40% of the full charge the evaporator can hold. However, this amount of water was chosen because it produces the maximum height of the water column in the refrigerant pool without touching the final tube. This way, the effect of pool boiling is not present, and the only heat transfer mechanism is falling-film. For the first evaporation phase ($M_{pool} > 0$), equation (13) is used to calculate $\dot{m}_{rec}$; when the pool is empty ($M_{pool} = 0$), $\dot{m}_{rec}$ is calculated with equation (14). To develop equations (13) and (14), the values of $\dot{m}_{rec}$ were measured from experimental tests, while the pressure difference (ΔP) and bottom refrigerant saturation temperature (T_{bot}) were estimated by knowing M_{pool}. The fitting procedure to determine the coefficients of equations (13) and (14) (presented in Table 2) was carried out in Matlab using the "cftool" command and the root-mean squares error method (RMSE). This way, $\dot{m}_{rec}$ was correlated with ΔP and T_{bot}, with 8910 Pa being the limiting value before entering the final transitory stage (i.e., changing from equation (13) to (14)). To smooth the transition between the two curves, the hyperbolic tangent is used, as presented in equation (15). A final aspect to highlight about equation (13), (14) and (15) is that the $\dot{m}_{rec}$ output is in $m^3\ h^{-1}$; with the use of the density, it can be switched to $kg\ s^{-1}$.

$$\dot{m}_{rec,1} = a_1 + \left(\frac{\Delta P - 9000}{53.36}\right) \cdot \left[a_2 + a_4 \cdot \left(\frac{\Delta P - 9000}{53.36}\right) + a_5 \cdot \left(\frac{T_{bot} - 10.90}{3.126}\right)\right] + a_3 \cdot \left(\frac{T_{bot} - 10.90}{3.126}\right) \tag{13}$$

$$\dot{m}_{rec,2} = b_1 \cdot \left(\frac{\Delta P}{8910}\right)^{b_2} \cdot \left(\frac{T_{bot} + 273.15}{647.096}\right) \tag{14}$$

$$\dot{m}_{rec} = \dot{m}_{rec,1} \cdot \left(0.5 \cdot \tanh\left(\frac{\Delta P - 8910}{17}\right) + 0.5\right) + \dot{m}_{rec,2} \cdot \left(1 - \left(0.5 \cdot \tanh\left(\frac{\Delta P - 8910}{17}\right) + 0.5\right)\right) \quad (15)$$

Table 2 – Recirculated flowrate correlations coefficients.

Coefficient	Value
a_1	0.1793
a_2	0.05213
a_3	-0.01643
a_4	-0.004222
a_5	-0.003321
b_1	0.1839
b_2	2.458

3.2 Energy balances and heat transfer model

3.2.1 Chilled water and film refrigerant energy balances

The energy balances were imposed to calculate the film's saturation temperature ($T_{ref,sat}$) and the outlet chilled water enthalpy ($h_{out,chw}$) and are presented in equations (16) and (17). The energy balance of equation (16) considers M_{film}, the generated mass of vapor (M_v) and the mass of the heat exchanger tubes (M_{HX}). The heat transferred from the chilled water to the refrigerant (Q_{evap}) is calculated according to equation (18). The overall heat transfer conductance (UA) was first presented in equation (3), as a function of variables calculated from experimental measurements; however, inside the model, thanks to the presence of the f_{wet} factor, the UA term can be calculated using all the thermal resistances, as detailed in equation (19). These thermal resistances are the chilled water forced conduction resistance (R_{chw}), cylinder wall conduction resistance (R_{wall}) and film heat transfer resistance (R_{film}). The chilled water heat transfer coefficient (h_{chw}) is calculated using Gnielinki's correlation (Gnielinski (1976)), as presented in equations (20) and (21) (for Reynolds numbers between 2300 and $5 \cdot 10^6$). The variable h_{chw} depends on the chilled water Reynolds and

Prandtl numbers (Re_{chw} and Pr_{chw}, respectively) as well as the friction factor f, calculated with equation (21).

$$\frac{dT_{ref,sat}}{dt} = \frac{-\dot{m}_{film,evap} \cdot \left(h_{fg}\right) + Q_{evap} - \frac{dM_v}{dt} \cdot \left(h_{fg} + Cp_{ref,sat} \cdot T_{ref,sat}\right)}{M_{film} \cdot Cp_{ref,sat} + M_v \cdot Cp_{ref,sat} + M_{HX} \cdot Cp_{HX}} \tag{16}$$

$$\frac{dh_{out,chw}}{dt} = \frac{\dot{m}_{chw} \cdot \left(h_{in,chw} - h_{out,chw}\right) - Q_{evap}}{M_{chw}} \tag{17}$$

$$Q_{evap} = \dot{m}_{chw} \cdot Cp_{chw} \cdot \left(T_{in,chw} - T_{ref,sat}\right) \cdot \left(1 - \exp\left(-\frac{UA}{\dot{m}_{chw} \cdot Cp_{chw}}\right)\right) \tag{18}$$

$$UA = \left(R_{chw} + R_{wall} + R_{film}\right)^{-1} = \left(\frac{1}{h_{chw} \cdot A_{int}} + \frac{Ln\left(\frac{D_{ext}}{D_{int}}\right)}{2 \cdot \pi \cdot L \cdot \lambda_{HX}} + \frac{1}{\bar{h}_{film} \cdot f_{wet} \cdot A_{ext}}\right)^{-1} \tag{19}$$

$$Nu_{chw} = \frac{\left(\frac{f}{2}\right) \cdot \left(Re_{chw} - 1000\right) \cdot Pr_{chw}}{1 + 12.7 \cdot \left(\frac{f}{2}\right)^{0.5} \cdot \left(Pr_{chw}^{\frac{2}{3}} - 1\right)} \tag{20}$$

$$f = 0.078 \cdot \left(Re_{chw}\right)^{-\frac{1}{4}} \tag{21}$$

3.2.2 Film heat transfer coefficient

The two main variables from equation (19) that are directly related to the refrigerant film are the wettability factor (f_{wet}) and the film heat transfer coefficient (h_{film}). The correlation used for the calculation of f_{wet} is one of the results of this study, and it is presented in section 4.1. On the other hand, as was presented in the introduction of this article, there are available several correlations to calculate h_{film}, but those correlations were developed under specific experimental conditions and for specified ranges of Re_{Γ}, which means that they can be out of range if used to validate the model for this falling-film evaporator.

Moreover, the calculation of h_{film} depends on if the film is in laminar or turbulent regime and needs to include the influence of the wettability of the tubes. For this model, h_{film} was calculated using Nusselt's classic theory for falling-film, with the use of the saturated film's thickness and thermal conductivity ($\lambda_{ref,sat}$), as expressed in equation (22).

$$h_{film}(\theta_i) = \frac{\lambda_{ref,sat}}{\delta_{film}(\theta_i)} = \lambda_{ref,sat} \cdot \left(\frac{3 \cdot \mu_l \cdot \left(\frac{\Gamma}{f_{wet}} \right)}{\rho_l \cdot (\rho_l - \rho_v) \cdot g \cdot \sin(\theta_i)} \right)^{-\frac{1}{3}} \quad (22)$$

The choice of equation (22) assumes that heat is transferred by conduction across the film and that the falling-film is laminar. According to the analyses presented in the introduction from Sarma and Saibabu (1992) and Chyu and Bergles (1987), the Nusselt conduction model holds for laminar films and, furthermore, in the fully developed region. The change from one heat transfer region to another in the outside of the tube is marked by the angular sector; in the introduction it was reported that Sarma and Saibabu (1992) obtained that, for a Re_Γ of 200 and assuming a fully wetted surface, the zone of simultaneous superheating and evaporation began at an angle of approximately 50°. For the case of sensible heat transfer, Zhao et al. (2022) stated that, when the film reaches the fully developed laminar flow regime, the film thickness becomes the determinant parameter for the heat transfer across the liquid layer and, in this case, the film thickness is inversely proportional to the heat transfer coefficient.

Considering the laminar/turbulent ranges presented in the introduction and that the experimentally obtained Re_Γ values are in a range of 120 – 4.5 (calculated with $\dot{m}_{rec}$ and equation (29), discussed in section 4.1) and in a range of 200 – 20 if a wetted length is considered (i.e., equation (29) divided by the obtained f_{wet} values, see section 4.1), the first remark to be made is that the falling-film flow can be considered in the laminar range and Nusselt's equation for film thickness (equation (11)) can be used.

For the case of equation (22), an assumption must be made. Without the exact knowledge of the peripheral angle where the film becomes fully developed and considering both, the calculated Re_Γ numbers and the results from Sarma and Saibabu (1992), equation (22) is used under the assumption that, for the laminar flow, all heat is transferred by means of conduction through the film with simultaneous superheating and

evaporation beginning at a peripheral angle below 50° (it was set to divide the tube in six angular sectors from 30° until 180°). When the average value of h_{film} is obtained, it is then multiplied by the wetted area, A_{wet}, to finally calculate the film thermal resistance, as presented in equation (23).

$$R_{film} = \frac{1}{\bar{h}_{film} \cdot A_{wet}} = \frac{1}{\bar{h}_{film} \cdot A_{ext} \cdot f_{wet}} \tag{23}$$

3.3 Vapor model

The final three equations that compose the ODE system are the vapor's volume, mass and temperature, respectively presented in equations (24), (25), and (26).

$$\frac{dV_v}{dt} = \frac{dV_{HX}}{dt} - \frac{dV_{pool}}{dt} - \frac{dV_{suction}}{dt} = -\frac{1}{\rho_l} \cdot \left(\frac{dM_{pool}}{dt} + \frac{dM_{suction}}{dt} \right) \tag{24}$$

$$\frac{dM_v}{dt} = \begin{cases} 0, & M_{film} > M_{film,transt} \\ \dot{m}_{evap,film} - \dot{m}_{evap,valve}, & M_{film} < M_{film,transt} \end{cases} \tag{25}$$

$$\frac{dT_v}{dt} = \begin{cases} \dfrac{dT_{ref,sat}}{dt}, & M_{film} > M_{film,transt} \\ \dfrac{\dfrac{dM_v}{dt} - \dfrac{dV_v}{dt} \cdot \left(\dfrac{P_v}{R_m\, T_v} \right)}{\left(\dfrac{V_v}{R_m} \right) \cdot \dfrac{d}{dT_v} \left(\dfrac{P_v}{T_v} \right)}, & M_{film} < M_{film,transt} \end{cases} \tag{26}$$

In equation (24), the term V_{HX} refers to the empty volume inside the evaporator. In equation (26), P_v is the vapor pressure, while R_m is the gas constant. The term $\dot{m}_{evap,valve}$ represents the evaporated flowrate that passes the valve and reaches the adsorption bed. For the entire quasi-steady-state section, equation (25) is equal to zero ($\dot{m}_{evap,film} = \dot{m}_{evap,valve}$); however, after reaching a transition point ($M_{film,transt}$), its value is constant and negative, meaning that there's a difference between $\dot{m}_{evap,film}$ and $\dot{m}_{evap,valve}$ (this hypothesis is further explained in section 4.3). This transition point also affects T_v in equation (26)..

3.4 Model f_{wet} identification equation

The expressions to identify f_{wet} from experimental data are presented in equations (27) and (28), and were derived considering that, only during the plateau section of the process, the experimental heat transfer rate Q_{exp} (equation (1)) is equal to Q_{evap} (equation (18)). Considering what was previously shown in equation (22), the term ξ, introduced in equation (27) and calculated with equation (28), can be defined as a film heat transfer parameter without considering the wetted surface.

$$f_{wet} = \left\{ \xi \cdot \left[\left(-C_{chw} \cdot Ln\left(1 - \frac{Q_{exp}}{C_{chw} \cdot \left(T_{in,chw} - T_{ref,sat} \right)} \right) \right)^{-1} - R_{chw} - R_{wall} \right] \right\}^{-\frac{3}{4}} \tag{27}$$

$$\xi = \lambda \cdot A_{ext} \cdot \left(\frac{3 \cdot \mu_l \cdot \dot{m}_{rec}}{4 \cdot \rho_l \cdot (\rho_l - \rho_v) \cdot g \cdot L_{tube}} \right)^{-\frac{1}{3}} \cdot \left(\frac{1}{6} \sum_{i=1}^{6} \left(\frac{1}{\sin(\theta_i)} \right)^{-\frac{1}{3}} \right) \tag{28}$$

4. Results and analysis

In this section, the f_{wet} correlation development is first presented. The data used to calibrate the correlation comes from a $T_{in,chw}$ range of 15 to 25 °C. After this, the model results concerning the UA parameter and $T_{ref,sat}$ are shown. Finally, the model's validation is detailed, as well as the hypothesis concerning the vapor's mass and temperature when the refrigerant pool is empty.

4.1. f_{wet} identification results

In Figure 4, the obtained f_{wet} curves for $T_{in,chw}$ of 15 and 25 °C are presented.

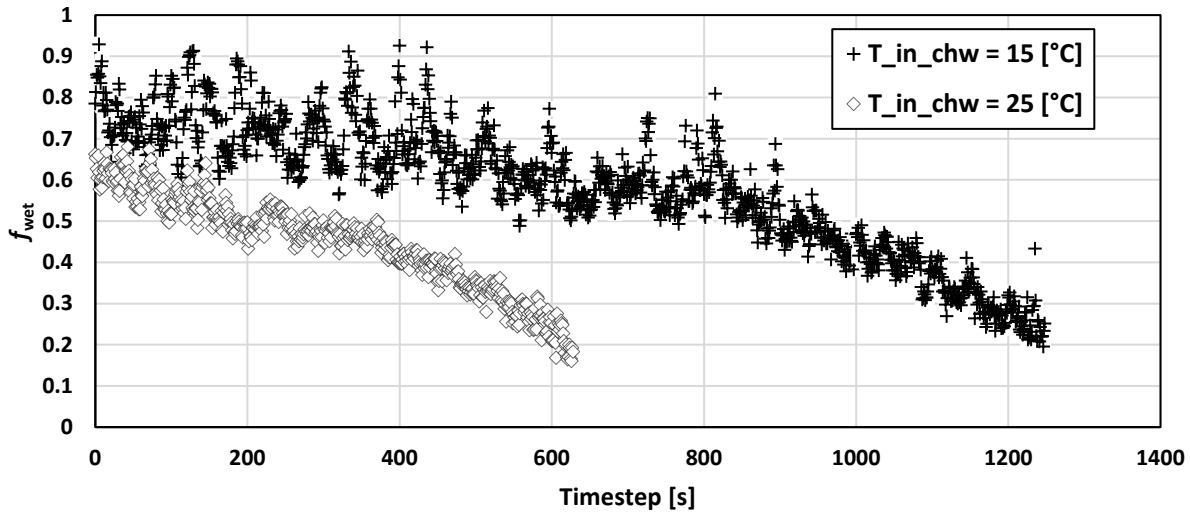

Figure 4 – f_{wet} identified curves.

As can be seen from Figure 6, the higher the $T_{in,chw}$, the lower the f_{wet} values. This can be explained as the combination of two factors: first, increasing $T_{in,chw}$ means that the pressure difference between the evaporator and the one in the adsorption bed increases as well (i.e., the pressure difference between the evaporator and adsorption bed at a $T_{in,chw}$ of 25 °C is higher compared to that obtained with $T_{in,chw}$ of 20 or 15 °C). Considering that all experimental tests were performed with an adsorption bed's temperature of 25 °C (see Table 1), the increase of the evaporator pressure means in a higher pressure difference and thus, a more intense evaporation. The second factor to consider is that, as both $T_{in,chw}$ and $T_{ref,sat}$ increase, the film's viscosity decreases, producing a thinner film on top of the tubes. A thinner film means a lower film

resistance. This result of a lower f_{wet} with the increase of $T_{ref,sat}$ was also seen in literature (Bustamante et al. (2020b); He et al. (2021); Zhao et al. (2022); LYu et al. (2018)).

To understand from the experimental tests if the falling film on top of the tubes was on a laminar or turbulent regime, the experimental Re_Γ values were calculated with equation (29), using $\dot{m}_{rec}$ instead of $\dot{m}_{out}$. The value of $\dot{m}_{out}$ was not used because, when gathering experimental data, it was unknown, and it depended on the f_{wet} term. The resulting range for Re_Γ values were, respectively, for 15 and 25 °C: 120 – 4.5 and 114 – 4.8. When considering a wetted length for equation (29) with the knowledge of the f_{wet} values, the resulting ranges were, respectively, for 15 and 25 °C: 180 – 20 and 200 – 20. Compared to the values seen in literature, this permits to establish that the film is in laminar regime and, therefore, the film's thickness (δ_{film}) becomes an important variable for the heat transfer through the liquid layer (conduction through the film). This way, as equation (22) shows, h_{film} is inversely proportional to Re_Γ.

For the development of the f_{wet} correlation, it was considered that f_{wet} depended on the following main inputs: the mass of film on top of the tubes and the film's temperature. The mass of film can be represented using the film Reynolds number (Re_Γ) from equation (29), calculated with $\dot{m}_{out}$ (equation (10)), while the temperature's influence can be inserted through the Prandtl number referred to the saturated refrigerant (Pr). Using Re_Γ as input for the calculation of f_{wet} is an idea that can also be found in literature (Ribatski and Thome (2007); Bustamante et al. (2020b); Habert and Thome (2010); LYu et al. (2018)). The data from the 15 and 25 °C tests was fitted into equation (30) using the root-mean squares error method (RMSE) in Matlab. The range for equation (30) includes Re_Γ values from 120 until 5 (always in laminar range, excluding low Re_Γ values), and $T_{in,chw}$ from 15 to 25 °C. The coefficients a_f, b_f and c_f are equal to 0.0072, 0.4583 and 0.9998, respectively.

$$Re_\Gamma = \frac{4 \cdot \Gamma}{\mu_{ref,sat}} \tag{29}$$

$$f_{wet} = (a_f) \cdot (Re_\Gamma)^{(b_f)} \cdot (Pr)^{(c_f)} \tag{30}$$

By introducing the expression for $\dot{m}_{out}$ in equation (29), equation (30) can be re-written as equation (31), where the direct link between f_{wet} and M_{film} is explicitly seen. The term $M_{film,cons}$ from equation (31) is shown in equation (32).

$$f_{wet} = \left(a_f \cdot Pr^{c_f}\right)^{\frac{1}{1+2b_f}} \cdot \left(\frac{M_{film}}{M_{film,cons}}\right)^{\frac{3b_f}{1+2b_f}} \tag{31}$$

$$M_{film,cons} = \left(\frac{\frac{3}{8} \cdot \mu_l^2 \cdot (12 \cdot A_{tube} \cdot \rho_l)^3 \cdot \left(\frac{1}{6} \cdot \sum_{i=1}^{6} \left(\frac{1}{\sin(\theta_i)}\right)^{\frac{1}{3}}\right)^3}{\rho_l \cdot (\rho_l - \rho_v) \cdot g}\right)^{\frac{1}{3}} \tag{32}$$

4.2. Model results and validation

The model results were validated against experimental data, and Figure 7 presents the comparison between the model and experimental data for $T_{ref,sat}$ while Figure 8 presents the comparison for UA. Figure 9 presents the f_{wet} correlation results. It is important to highlight that the following figures also include the model results with a $T_{in,chw}$ of 20 °C. As previously seen in Figure 6, the correlation for f_{wet} was developed using the data from the tests at 15 and 25 °C, so testing the model with an inlet chilled water temperature inside that interval (20 °C) and obtaining accurate results provides further validation for the developed correlations and the model.

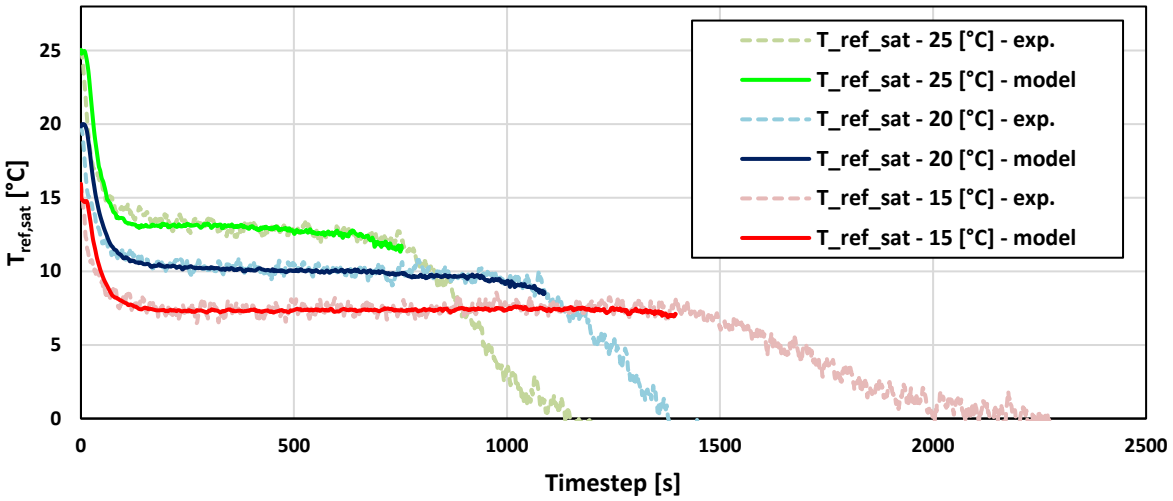

Figure 5 – Film saturation temperature comparison.

As can be seen from Figures 7 and 8, the model is able to closely replicate experimental data during the quasi steady-state section of the process ($M_{pool} > 0$). Both $T_{ref,sat}$ and UA, as well as the evaporation dynamics, depend on the accuracy of f_{wet}, so both figures confirm that the trend obtained for f_{wet} was correct. Following the results from Figure 7, once the steady-state section is over ($M_{pool} = 0$), the saturation temperature begins to decrease, meaning that the amount of refrigerant that falls into the tubes is no longer enough to keep the process going under quasi steady-state conditions. This marked the beginning of the final transition stage.

The final transitory stage (a particular situation for this single-bed adsorption chiller) is a phase of the evaporation process in which the refrigerant pool is empty, and the pump sends the remaining refrigerant in the aspiration tube to the top of the evaporator. As fewer refrigerant falls on top of the tubes, the dry patches continue to increase, producing a decline in the performance of the evaporator, where the UA decreases until reaching zero (see Figure 8). Compared to a real operating situation, this is a state that must be avoided because the adsorption chiller should provide a continuous cooling effect if there are cooling loads to be met. Even though at this point of $M_{pool} = 0$ it was clear that the pump struggled to send the remaining refrigerant to the top of the evaporator, a new hypothesis, explained in section 4.3, was formulated due to the uncertainty surrounding the real conditions of the refrigerant vapor inside the evaporator. It was not considered correct to assume that, at this final stage, the refrigerant vapor temperature could still be

calculated with equation (16), and early testing of the model provided wrong saturation temperature behaviors once the final transition stage was reached. Instead, this final stage required the use of equation (26) and the explanations of section 4.3.

Therefore, to motivate the need for a vapor model and a new hypothesis during the phase when $M_{pool} = 0$, the model curves for the saturation temperature are presented until the end of the steady-state section for Figure 7 only. The rest of the figures presented in this section already contemplate the hypothesis from section 4.3 and the change from equation (16) to equation (26) at the final transition stage.

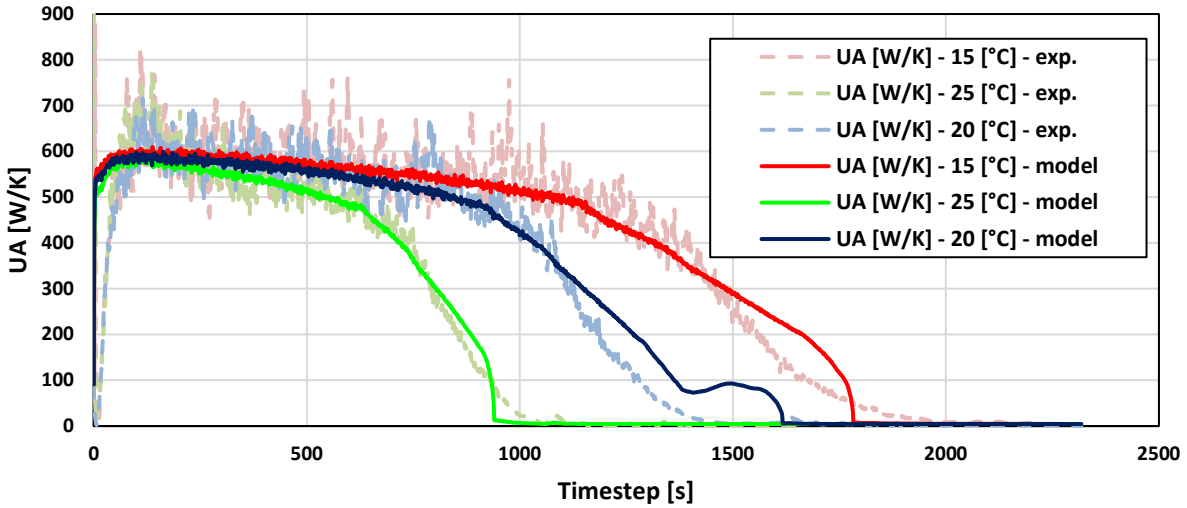

Figure 6 – Overall heat transfer conductance (UA) comparison.

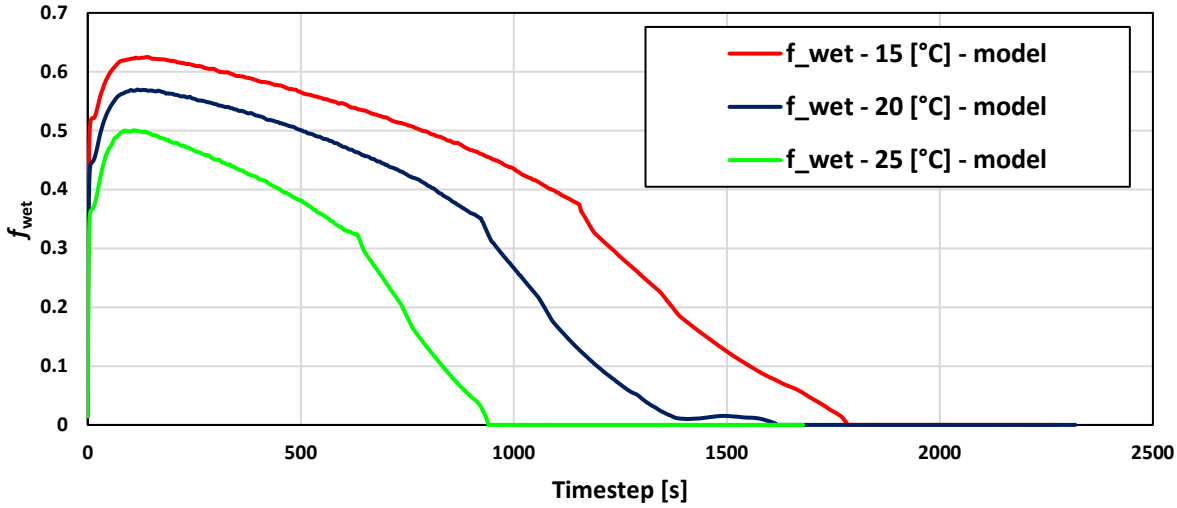

Figure 7 – f_{wet} model results with developed correlation.

The f_{wet} curves from Figure 7 have an initial increase due to the increase of M_{film} (initial transient phase), and then this is followed by a continuous decrease in the quasi steady-state section; when M_{pool} = 0, the f_{wet} curves have a steeper decrease, until reaching a minimum value. The results of Figures 6 and 7 confirm that the reduction of UA is due to the continuous reduction of the film flowrate and wetted surface. This means that the f_{wet} factor is the main driver of the evaporation process and, to ensure the proper evaporator's performance, the amount of refrigerant in the pool has to be maintained above a certain limit (Toppi et al. (2022)). During the final transition stage (M_{pool} = 0), the Re_{Γ} numbers are below 5 and equation (31) is out of range. Even though equation (31) may provide reasonable results by having f_{wet} following the decrease of M_{film}, there is no guarantee that the Nusselt's film thickness correlation, based on $\dot{m}_{out}$, is still valid at very low Re_{Γ}, and this can produce numerical inaccuracies at the end, as seen in Figure 8 for $T_{in,chw}$ = 20 °C.

4.3 Final transition stage and hypothesis for vapor's mass and temperature when M_{pool} = 0

As first presented in section 4.2, the final transitory stage (M_{pool} = 0 and $\dot{m}_{rec} \sim 0$) required the introduction of a final hypothesis due to the uncertainty surrounding the process' physics inside the evaporator when the evaporator pressure begins to decrease. It can be thought that, at this point, capillary forces hold the small remaining mass of film in the spaces between consecutive fins, but the adsorption bed continues to extract vapor from the evaporator. This leads to a disassociation between the produced refrigerant vapor flowrate and the one effectively crossing the valve to the adsorption bed, affecting the readings from the pressure transducer. This final hypothesis that contemplated the rupture of the link between $\dot{m}_{film,evap}$ and $\dot{m}_{evap,valve}$ from equation (25) was inserted in the model and produced the desired behavior from the vapor temperature, T_v. The value of T_v is equal to $T_{ref,sat}$ if M_{film} is higher than a transition value ($M_{film,transt}$); however, below this value, T_v is calculated with the ideal gas equation and it depends on equation (25), which is re-written as equation (33), imposing a constant (and negative) decrease of the change of the mass of vapor, represented by a constant variable K_v. This variable K_v was calibrated with the experimental data. To illustrate this, T_v is presented in Figure 10 for $T_{in,chw}$ of 15 °C.

$$\frac{dM_v}{dt} = \dot{m}_{evap,film} - \dot{m}_{evap,valve} = -K_v = -3.68 \cdot 10^{-8} \quad (33)$$

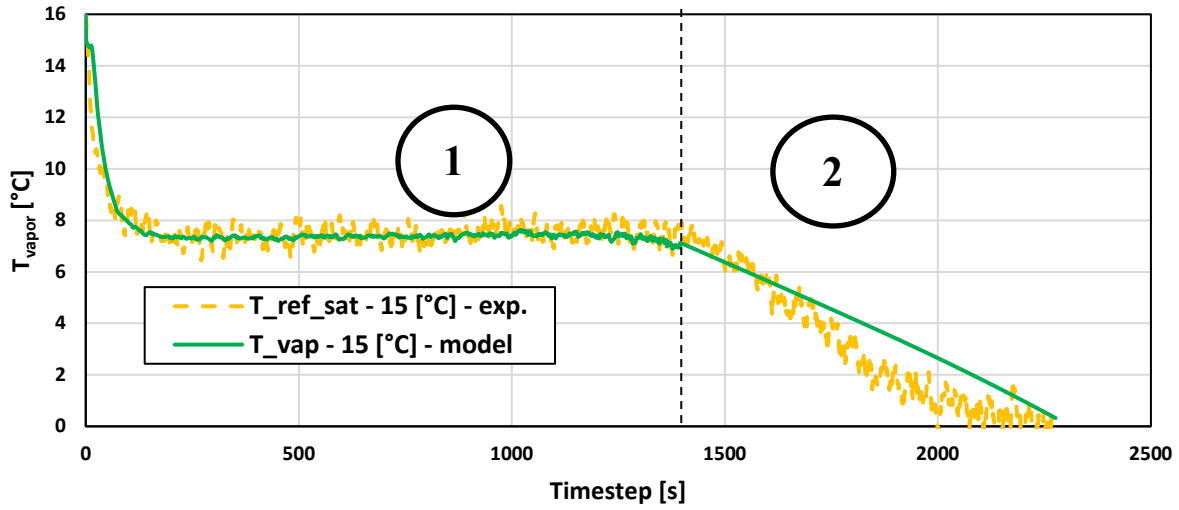

Figure 8 – Vapor temperature with $T_{in,chw}$ of 15 °C.

From Figure 10, it can be analyzed that, for the quasi-steady-state operation of the evaporator (identified with number 1), the vapor is under saturation conditions, meaning that its temperature is calculated with equation (16). Also, at this stage, equation (33) is equal to zero. However, when the process enters the final transition stage (section 2 in Figure 10) with M_{pool} = 0 and $\dot{m}_{rec} \sim 0$, there is not enough refrigerant falling on top of the tubes to ensure a continuous process; this further increases the dry patches on the surface of the tubes and leads to a more marked decrease of the overall UA conductance.

To explain and model the continuous decrease of the pressure and temperature, it was hypothesized, as previously stated, that on the final transitory stage there was a rupture between the produced vapor flowrate and the one that is effectively extracted towards the adsorption bed. At this point in section 2 (see Figure 8), the vapor temperature does not follow equation (16) but decreases following an ideal gas model from equation (26), which, at the same time, depends on equation (33). As the adsorption bed continuous to extract more vapor, the pressure inside the evaporator continues to decrease on each timestep (and the remaining fraction of film is thought to be held by capillary forces between the spaces of consecutive fins).

The analyses from Figures 7 to 10 also allow to establish that this dynamic model can then be used to identify and predict the moment the refrigerant pool is empty. This information can also be used in future research to adapt a control strategy where a given amount of refrigerant from the condenser can be

discharged into the evaporator once the pool is below a certain limit, to avoid entering the final transition phase.

5. Conclusions

A dynamic model was developed to simulate the evaporation process of a prototype falling-film evaporator that is part of a single-bed adsorption chiller test bench. The experimental data used for its calibration came from tests performed on the test bench under realistic operating conditions, which allowed to better represent real evaporation dynamics in the model. Furthermore, a correlation to calculate the effective wetted area was also developed; for this, a variable called wettability factor (f_{wet}) was introduced and its values were estimated starting from experimental data. The model results and subsequent validation allowed to obtain the following conclusions:

- The accuracy of the wetted surface prediction through the f_{wet} correlation is key for obtaining realistic results of UA and $T_{ref,sat}$ (accurate evaporation dynamics). Therefore, the evolution of the wetted surface represented by the f_{wet} factor is the main driver of the evaporation process.
- The continuous decrease of wetted surface and film flowrate leads to a decrease of the UA value. This confirms the conclusions obtained by Toppi et al. (2022) on a separate research on the same adsorption chiller test bench.
- As $T_{in,chw}$ increased, the identified f_{wet} values with the model were lower. For 15 °C, the f_{wet} range was of 0.80 – 0.20, while for 25 °C the range was of 0.60 – 0.20.
- The final transition stage required an extra hypothesis for the analysis of the vapor's mass and temperature. The hypothesis was focused on the rupture of the link between the effective vapor flowrate passing to the adsorption bed and the flowrate produced by the mass of film on top of the tubes. Furthermore, during the final stage of the process, the f_{wet} correlation is out of range because of very low Re_{Γ} values. To avoid entering on these situations and to ensure the proper evaporator's performance, the amount of refrigerant in the pool has to be maintained above a certain limit.
- This previous final idea means that, for future research, a control strategy can be developed to discharge water from the condenser once the refrigerant pool is below a certain limit. This changes

the energy and mass balances of the evaporator but can serve to understand how to maintain a continuous evaporation process for a longer time and avoid entering in the final transition stage.

Nomenclature

A_{ext}	Total external area, m^2
A_{tube}	External area of one tube, m^2
C_{chw}	Chilled water heat capacity rate, W K^{-1}
Cp	Specific heat capacity, kJ kg^{-1} K^{-1}
D	Diameter, m
f	Friction factor for Gnielinski correlation, dimensionless
f_{wet}	Wettability factor, dimensionless
g	Gravity, 9.8 m s^{-2}
h_{chw}	Chilled water heat transfer coefficient, W m^{-2} K^{-1}
h_{fg}	Heat of evaporation, kJ kg^{-1}
h_{film}	Refrigerant film heat transfer coefficient, W m^{-2} K^{-1}
$h_{out,chw}$	Chilled water outlet enthalpy, kJ kg^{-1}
K_v	Constant value for the derivative of the mass of vapor, kg s^{-1}
L	Total external length, m
L_{tube}	Length of one tube, m
$M_{discharge}$	Refrigerant mass in the pump's suction tube, kg
$M_{film,cons}$	Constant mass of film term, kg
$M_{film,transt}$	Transition mass of film, kg
M_{film}	Film refrigerant mass, kg
M_{pool}	Pool refrigerant mass, kg
$M_{suction}$	Refrigerant mass in the pump's suction tube, kg
M_v	Vapor mass, kg
$\dot{m}_{chw}$	Chilled water flowrate, m^3 h^{-1}

$\dot{m}_{evap,valve}$	Evaporated flowrate that passes the valve going to the adsorption bed, kg s^{-1}
$\dot{m}_{film,evap}$	Film evaporated flowrate, kg s^{-1}
$\dot{m}_{out}$	Film refrigerant falling back to the pool, kg s^{-1}
$\dot{m}_{rec}$	Recirculated flowrate, kg s^{-1}
Nu	Nusselt number, dimensionless
$P_{ref,sat}$	Refrigerant saturation pressure, Pa
Pr	Prandtl number, dimensionless
ΔP	Pressure difference between water's free surface and pump's inlet, Pa
Q_{evap}	Heat transferred from chilled water to refrigerant, W
Q_{exp}	Experimental heat transfer rate, W
R	Thermal resistance, K W^{-1}
R_m	Specific gas constant, kJ kg^{-1} K^{-1}
Re_Γ	Film Reynolds number, dimensionless
T_{bot}	Saturation temperature calculated at the bottom of the refrigerant's pool, °C
$T_{in,chw}$	Inlet chilled water temperature, °C
$T_{out,chw}$	Outlet chilled water temperature, °C
$T_{ref,sat}$	Refrigerant saturation temperature, °C
$T_{water,ads}$	Adsorption bed circulating water temperature, °C
ΔT_{LMTD}	Logarithmic mean temperature difference, K
UA	Overall heat transfer conductance, W K^{-1}
V	Volume, m^3

Subscripts

chw	Chilled water
ext	External
$film$	Refrigerant film
HX	Heat exchanger

int	Internal
l	Liquid
ref, sat	Saturated refrigerant
v	Vapor
$wall$	Cylinder wall
wet	Wetted

Greek symbols

δ	Film thickness, m
Γ	Film flow density, kg s^{-1} m^{-1}
θ	Peripheral angle, radians
λ	Thermal conductivity, W m^{-1} K^{-1}
μ	Dynamic viscosity, kg m^{-1} s^{-1}
ξ	Film heat transfer parameter without considering a wetted surface, W K^{-1}
ρ	Density, kg m^{-3}

References

Alhusseini, AA., Tuzla, K., Chen, J.C. 1998. Falling film evaporation of single component liquids. Int. J. Heat Mass Transf. 41(12), 1623-1632. doi: https://doi.org/10.1016/S0017-9310(97)00308-6.

Ammar, S.M., Park, C.W., 2021. Evaporation heat transfer characteristics of falling film in small diameter fabricated tubes of absorption refrigeration system: An experimental investigation. Int. J. Heat Mass Transf. 165, Part A, 120618. doi: https://doi.org/10.1016/j.ijheatmasstransfer.2020.120618.

Aprile, M., Freni, A., Toppi, T., Motta, M., 2020. Modelling and performance assessment of a thermally-driven cascade adsorption cycle suitable for cooling applications. Therm. Sci. Eng. Prog. 19, 100602. doi: https://doi.org/10.1016/j.tsep.2020.100602.

Bustamante, J.G., Garimella, S., Hughes, M., 2020a. Falling-Film evaporation over horizontal rectangular tubes: Part I – Experimental results. Int. J. Refrig. 119, 37-47. doi: https://doi.org/10.1016/j.ijrefrig.2020.07.018.

Bustamante, J.G., Garimella, S., Hughes, M., 2020b. Falling-Film evaporation over horizontal rectangular tubes: Part II – Modeling. Int. J. Refrig. 120, 188-199. doi: https://doi.org/10.1016/j.ijrefrig.2020.07.022.

Cao, C., Xie, L., He, X., Ji, Q., Zhao, H., Du. Y., 2022. Numerical study on the flow and heat transfer characteristics of horizontal finned-tube falling-film evaporation: Effects of liquid column spacing and wettability. Int. J. Heat Mass Transf. 188, 122665. doi: https://doi.org/10.1016/j.ijheatmasstransfer.2022.122665.

Chauhan, P.R., Kaushik, S.C., Tyagi, S.K., 2022. Current status and technological advancements in adsorption refrigeration systems: A review. Renew. Sust. Energ. Rev. 154, 111808. doi: https://doi.org/10.1016/j.rser.2021.111808.

Chun K.R., Seban, R.A., 1971. Heat transfer to evaporating liquid films. ASME J. Heat Transfer. 93(4), 391 – 396. doi: https://doi.org/10.1115/1.3449836.

Chyu, M.-C., Bergles, A., 1987. An analytical and experimental study of falling-film evaporation on a horizontal tube. J. Heat Transf. 109(4), 983 – 990. doi: https://doi.org/10.1115/1.3248214.

De la Calle, A., Yebra, L. J., Dormido. S., 2012. Modeling of a falling film evaporator. In: 9th International MODELICA Conference, Munich, Germany, Linköping Electronic Conference Proceedings, pp. 941-948, Linköping University Electronic Press. doi: http://dx.doi.org/10.3384/ecp12076941.

De la Calle, A., Yebra, L. J., Dormido. S., 2013. Dynamic Modeling and Simulation Study of Falling Film Evaporation and Condensation. In: 8th EUROSIM Congress on Modelling and Simulation (EUROSIM), pp. 472-432. doi: https://doi.org/10.1109/EUROSIM.2013.79.

Ding, H., Xie, P., Ingham, D., Ma, L., Pourkashanian, M. 2018. Flow behavior of drop and jet modes of a laminar falling film on horizontal tubes. Int. J. Heat Mass Transf. 124, 929-942. doi: https://doi.org/10.1016/j.ijheatmasstransfer.2018.03.111

Ganic, E.N., Roppo, M.N. 1980. An Experimental Study of Falling Liquid Film Breakdown on a Horizontal Cylinder During Heat Transfer. ASME J. Heat Transfer. 102(2), 342 – 346. doi: https://doi.org/10.1115/1.3244285

Gnielinski, V., 1976. New equations for heat and mass transfer in turbulent pipe and channel flow, Int. Chem. Eng., 16(2), pp. 359-368.

Guichet, V., Jouhara, H. 2020. Condensation, evaporation and boiling of falling films in wickless heat pipes (two-phase closed thermosyphons): A critical review of correlations. International Journal of Thermofluids 1 – 2. 100001. doi: https://doi.org/10.1016/j.ijft.2019.100001

Habert, M., Thome, J. R., 2010. Falling-Film Evaporation on Tube Bundle with Plain and Enhanced Tubes—Part II: New Prediction Methods. Exp. Heat Transf. 23(4), 281-297. doi: https://doi.org/10.1080/08916152.2010.502046.

Han, J.C., Fletcher, L.S., 1985. Falling film evaporation and boiling in circumferential and axial grooves on horizontal tubes. Ind. Eng. Chem. Process. Des. Dev. 24(3), 570 – 575. doi: https://doi.org/10.1021/i200030a009

He, Y., Xiong, K., Xia, E., 2021. Growth of dry patches in evaporating film flowing around a horizontal circular tube. Int. Commun. Heat Mass Transf. 125, 105291. doi: https://doi.org/10.1016/j.icheatmasstransfer.2021.105291.

Lee, W.S., Park, M.Y., Duong, X.Q., Cao, N.V., Chung, J.D., 2020. Effects of evaporator and condenser in the analysis of adsorption chillers. Energies. 13(8), 1901. doi: https://doi.org/10.3390/en13081901

LYu, Y., Yin, Y., Zhang, X., Jin, X., 2018. Investigation of falling-film plate wettabilitycharacteristics under dehumidification and regeneration conditions using LiCl-H2O. Int J Refrig. 94, 118-126. doi: https://doi.org/10.1016/j.ijrefrig.2018.07.002

Mitra, S., Srinivasan, K., Kumar, P., Murthy, S.S., Dutta, P., 2014. Solar driven Adsorption Desalination system. Energy Procedia. 49, 2261-2269. doi: https://doi.org/10.1016/j.egypro.2014.03.239.

Mitrovic, J., 1986. Influence of tube spacing and flow rate on heat transfer from a horizontal tube to a falling liquid film. In: Proc. 8th Int. Heat Transfer Conf., San Francisco, USA, vol. 4, pp. 1949-1956.

Mostafa, I., Jin, P.-.H., Zhang, Z., Tao, W.-.Q., 2020. Experimental study of the falling film evaporation coefficients of R290 in a horizontal enhanced tube array. Int. J. Heat Mass Transf. 159, 120099. doi: https://doi.org/10.1016/j.ijheatmasstransfer.2020.120099.

Muttakin, M., Islam, M.A., Malik, K.S., Pahwa, D., Saha, B.B., 2021. Study on optimized adsorption chiller employing various heat and mass recovery schemes. Int. J. Refrig. 126, 222-237. https://doi.org/10.1016/j.ijrefrig.2020.12.032.

Nayrana, D.-.P., Resch, A., 2021. Preliminary Results on Experimental Modelling of an Adsorption Chiller. Renew. Energy Environ. Sustain. 6(29), doi: https://doi.org/10.1051/rees/2021030.

Ouldhadda D., Il Idrissi, A. 2001. Laminar Flow and Heat transfer of non-Newtonian falling liquid film on a horizontal tube with variable surface heat flux. Int. Comm. Heat Mass Transfer. 28(8), 1125 – 1135. doi: https://doi.org/10.1016/S0735-1933(01)00315-3

Owens, W. L., 1978. Correlation of thin film evaporation heat transfer coefficients for horizontal tubes. In: Fifth Ocean Thermal Energy Conversion Conference, Miami Beach, Florida, pp. 71-89 VI-.

Pan, Q., Peng, J., Wang, R., 2019. Experimental study of an adsorption chiller for extra low temperature waste heat utilization. Appl. Therm. Eng. 163, 114341. doi: https://doi.org/10.1016/j.applthermaleng.2019.114341.

Parken, W.H., Fletcher, L.S. 1982. Heat transfer in thin liquid films flowing over horizontal tubes. In: Proc. 7th Int. Heat Transfer Conf, Munich, Germany, vol. 6, pp. 415 – 420.

Ribatski, G., Jacobi, A.M., 2005. Falling-film evaporation on horizontal tubes – a critical review. Int. J. Refrig. 28, 635-653. doi: https://doi.org/10.1016/j.ijrefrig.2004.12.002.

Ribatski, G., Thome, J.R., 2007. Experimental study on the onset of local dryout in an evaporating falling film on horizontal plain tubes. Exp. Therm. Fluid Sci. 31, 483-493. doi: https://doi.org/10.1016/j.expthermflusci.2006.05.010.

Roques, J.-F., Thome, J. R., 2007 Falling Films on Arrays of Horizontal Tubes with R-134a, Part II: Flow Visualization, Onset of Dryout, and Heat Transfer Predictions. Heat Transf. Eng. 28(5), 415-434. doi: https://doi.org/10.1080/01457630601163736.

Roumpedakis, T. C., Vasta, S., Sapienza, A., Kallis, G., Karellas, S., Wittstadt, U., Tanne, M., Harborth, N., Sonnenfeld, U., 2020. Performance Results of a Solar Adsorption Cooling and Heating Unit. Energies. 13(7), 1630. doi: https://doi.org/10.3390/en13071630.

Sarma, P.K., and Saibabu, J., 1992. Evaporation of laminar, falling liquid film on a horizontal cylinder. Wärme- und Stoffübertragung. 27, 347 – 355. doi: https://doi.org/10.1007/BF01600024

Sztekler, K., Kalawa, W., Nowak, W., Mika, L., Gradziel, S., Krzywanski, J., Radomska, E. 2020. Experimental Study of Three-Bed Adsorption Chiller with Desalination Function. Energies. 13(21), 5827. doi: https://doi.org/10.3390/en13215827.

Tahir, F., Mabrouk, A., Koc, M. 2021. Influence of co-current vapor flow on falling film over horizontal tube. Int. J. Therm. Sci. 159, 106614. doi: https://doi.org/10.1016/j.ijthermalsci.2020.106614

Thimmaiah, P.C., Sharafian, A., Rouhani, M., Huttema, W., Bahrami, M., 2017. Evaluation of low-pressure flooded evaporator performance for adsorption chillers. Energy. 122, 144 – 158. doi: https://doi.org/10.1016/j.energy.2017.01.085.

Toppi, T., Villa, T., Vasta, S., Mittelbach, W., Freni, A., 2022. Testing of a Falling-FilmEvaporator for Adsorption Chillers. Energies. 15, 1709. doi: https://doi.org/10.3390/en15051709.

Ueda, T., Tanaka, H. 1975. Measurements of velocity, temperature, and velocity fluctuation distributions in falling liquid films. Int. J. Multiph. Flow. 2(3), 261–272. doi: https://doi.org/10.1016/0301-9322(75)90014-2

Volmer, R., Eckert, J., Fuldner, G., Schnabel. L., 2017. Evaporator development for adsorption heat transformation devices – Influencing factor on non-stationary evaporation with tube- fin heat exchangers at sub-atmospheric pressure. Renew. Energy. 110, 141-153. doi: https://doi.org/10.1016/j.renene.2016.08.030

Yang, L., Song, X., Xie, Y., 2017. Effect of the Dryout in Tube Bundles on the Heat Transfer Performance of Falling Film Evaporator. Procedia Eng. 205, 2176-2183. doi: https://doi.org/10.1016/j.proeng.2017.10.041.

Zhao, C.-.Y., Qi, D., Ji, W.-.T., Jin, P.-.H., Tao, W.-.Q., 2022. A comprehensive review on computational studies of falling film hydrodynamics and heat transfer on the horizontal tube and tube bundle. Appl. Therm. Eng. 202, 117869. doi: https://doi.org/10.1016/j.applthermaleng.2021.117869.

Ziegler, F., 2009. Sorption heat pumping technologies: Comparisons and challenges. Int. J. Refrig. 32(4), 566-576. doi: https://doi.org/10.1016/j.ijrefrig.2009.03.007.